

Learning nuclear cross sections across the chart of nuclides with graph neural networks

Sinjini Mitra*

Geometric Media Lab, Arizona State University, 1151 S Forest Ave. Tempe, AZ 85281

Hongjun Choi[†] and Shusen Liu[‡]

*Machine Intelligence Group, Center for Applied Scientific Computing,
Lawrence Livermore National Laboratory, Livermore, California 94551, USA*

Ruben Glatt[§]

*Machine Learning Group, Computational Engineering Division,
Lawrence Livermore National Laboratory, Livermore, California 94551, USA*

Kyle Wendt[¶] and Nicolas Schunck^{**}

*Nuclear Data and Theory Group, Nuclear and Chemical Sciences Division,
Lawrence Livermore National Laboratory, Livermore, California 94551, USA*

(Dated: February 21, 2025)

In this work, we explore the use of deep learning techniques to learn how nuclear cross-sections change as we add or remove protons and neutrons. As a proof of principle, we focus on the neutron-induced reactions in the fast energy regime that are the most important in nuclear science and engineering. We use variational autoencoders (VAEs) and implicit neural representations (INRs) to build a learned feature representation space of nuclear cross sections and reduce the dimensionality of the problem. We then train graph neural networks (GNNs) on the resulting latent space to leverage the topological information encoded in the chart of isotopes and to capture the variations of cross sections with the number of particles in nuclei. We find that hypernetworks based on INRs significantly outperforms VAEs in encoding nuclear cross-sections. This superiority is attributed to INR’s ability to model complex, varying frequency details, which enables lower prediction errors when combined with GNNs. We also observe that GNN optimization is much more successful when performed in the latent space, whether using INRs or VAEs. However VAEs’ continuous representation also allows for direct GNN training in the original input space. We leverage these representational learning techniques and successfully predict cross sections for a 17×17 block of nuclei with high accuracy and precision. Using clustering algorithms, we map groups of latent vectors into regions of the nuclear chart and show that VAEs and INRs can discover some of the neutron magic numbers. These findings suggest that deep-learning models based on representation encoding of cross-sections combined with graph neural networks hold significant potential in augmenting nuclear theory models, e.g., providing reliable estimates of covariances of cross sections, including cross-material covariances.

I. INTRODUCTION

Nuclear cross sections encode the probability of a subatomic particle to interact with an atomic nucleus, defined by its proton and neutron numbers (Z, N) [1]. Each atomic nucleus can be involved in many different types of nuclear reactions often simply denoted as (*incoming process, outgoing process*), also called “channels”. For example, the (n, γ) channel involves the absorption of a neutron and the emission of one or several photons (γ rays) while the (n, f) channel involves the absorption of a neutron resulting in the fission of the nucleus. Nuclear reaction libraries are formed by the set of all known

cross sections for all known nuclei [2–4]. Such libraries are essential inputs to nuclear technology applications [5], which include energy production [6], nuclear medicine [7], and nuclear forensics [8]. They also play a critical role in our attempts at understanding the formation of elements in the universe [9, 10]. The importance of such libraries, and of nuclear data in general, in scientific research, was recently underlined in the 2023 Long Range Plan for Nuclear Science commissioned by the U.S. Department of Energy and the National Science Foundation [11].

Measuring nuclear cross sections requires complex and expensive experimental facilities and is often impossible for short-lived radioactive nuclei that cannot be made as targets. While nuclear reaction theory has greatly improved over the past decades [12], its level of sophistication varies greatly depending on the nucleus and type of reaction. In very light nuclei, *ab initio* theory can successfully describe reactions at low energy in a fully quantum-mechanical framework [13]; in contrast, reactions of heavy nuclei with neutrons with just a few sub-eV energy already lead to the formation of a highly excited

* smitra16@asu.edu

† choi22@llnl.gov

‡ liu42@llnl.gov

§ glatt1@llnl.gov

¶ wendt6@llnl.gov

** schunck1@llnl.gov

nucleus with an extremely complex structure that can only be described within a statistical framework [14, 15]. In practice, such statistical reaction theory relies on additional theoretical inputs describing nuclear properties such as the nuclear level density, the probability of capturing incident particles, the rate of decay through the emission of photons, neutrons, protons, etc. [16]. Today the best nuclear data libraries on the market largely rely on phenomenological models to determine such properties. These models are carefully calibrated to match realistic application requirements such as the criticality regimes of a nuclear reactor, at the price of a loss in generality and predictive power of the underlying theory [4, 17]. As a result, current models fail at consistently predicting the complex relationships between different types of cross sections in a single nucleus, or between cross sections in different nuclei across the chart of isotopes. This lack of predictive power is a significant impediment to efforts at designing new, cleaner or more efficient nuclear technologies. While research in fundamental reaction theory continues to progress, techniques originating from artificial intelligence and machine learning research offer an alternative viewpoint [18–21].

Indeed, each single cross section is a continuous one-dimensional function of the energy of the incident particle akin to a time sequence labeled by the number of protons Z and neutrons N . In neutron-induced reactions in the fast regime – when the energy E of the incident neutron is $E > 100$ keV – cross sections are rather smooth functions of neutron energy (notwithstanding threshold effects). Therefore, dimensionality reduction techniques could in principle be applied to compress information and learn from the data the physically relevant latent space that underpin the cross sections.

In addition, cross sections of nuclei with close (Z, N) numbers often tend to have similar forms suggesting a correlation with the position on the 2D grid structure spanned by Z and N . This observation suggests employing geometric deep learning for learning meaningful representations in the latent space, a technique that has recently emerged as an impactful sub-field adept at learning non-Euclidean sub-spaces [22]. Graph Neural Networks (GNNs) [23] in particular, provide an easy way to perform node-level, edge-level, and graph-level prediction tasks while being permutation invariant for structured grid-like data in such non-Euclidean sub-spaces, as has been shown for particle reconstruction [24].

The goal of this paper is to expose the intricate relationships between cross sections of different nuclei by leveraging such state-of-the-art deep learning models. To this end, we employ two complementary techniques in succession. As the first step, we use either a variational autoencoder (VAE) [25] or an implicit neural representation (INR) to uncover the latent space of nuclear cross sections and reduce the dimensionality of the problem. In the second step, we use GNNs operating on such latent spaces to predict how cross sections transform when adding a neutron or a proton to a nucleus (Z, N) in order

to account for the implicit 2D geometric nature of the nuclear chart. The resulting network provides an efficient, consistent framework to predict unknown cross sections not too far from the training region.

This paper is organized as follows: Section II gives a broad overview of the challenges facing nuclear theory when computing nuclear data. In Section III, we summarize the main aspects of our theoretical approach including the architecture of the network and the characteristics of the datasets used for training. Section IV shows the results for different GNN architectures and encoder approaches. Section V discusses our results in the context of related work on nuclear data before we summarize our findings in Section VI.

II. THEORETICAL MODELS OF NUCLEAR DATA: CHALLENGES

As mentioned in the introduction, nuclear reaction libraries are formed by the set of all known cross sections for all known nuclei. Most of this data is not simply a set of experimental data points but the result of an *evaluation* of all available data by subject matter experts. This evaluation is itself the outcome of a complex, multi-stage, iterative process that involves: (i) carefully analyzing available experimental results (vetting outliers, estimating uncertainties, etc.) (ii) adjusting model parameters of nuclear reaction codes such as TALYS [26] or EMPIRE [27] in such a way that the cross sections computed with such codes “match”, or are close to, experimental measurements (iii) *processing* the data (energy binning, heating of cross sections to room temperature values, etc.) (iv) verifying the nuclear reaction library through *benchmarks*, e.g., running a suite of codes simulating critical assemblies.

From a physics perspective, nuclear reactions are extremely complex processes. Ideally, one would like to describe any reaction as a quantum-mechanical evolution from an initial state, e.g., an incoming particle a with energy E_a , spin J_a and parity π_a impinging on a target at rest A with energy E_A , spin J_A and parity π_A , to a final state such as two reaction products b and B with respective energies E_b (E_B), spins J_b (J_B) and parities π_b (π_B). Doing this would require the perfect characterization of the quantum-mechanical state of all reaction products a , A , b and B as well as the exact knowledge of the nuclear many-body Hamiltonian \hat{H} , since the unitary quantum-mechanical time evolution operator is $e^{-i\hat{H}t/\hbar}$. Both are out of reach of current nuclear theory.

In practice, the physics of a nuclear reaction is instead described by a suite of models with varying degrees of sophistication and phenomenology. These models play an essential role in the evaluation process and can be divided into several broad categories: (i) optical models describe the interaction of an incoming particle a with a target A (ii) level density models characterize the number of available energy levels $\rho(E, J, \pi)$ at a given ex-

citation energy E , angular momentum J and parity π (iii) gamma-strength functions $\gamma_{SF}(E)$ characterize the probabilities of emitting photons as a function of energy E (iv) fission transmission coefficients quantify the probability for a (heavy) nucleus to undergo fission as a function of energy, angular momentum and parity (v) pre-equilibrium reaction models describe interaction mechanisms between projectile and target that involve specific nuclear excited states.

All these models are but different facets of the ideal quantum-mechanical evolution describe above. This implies that they should all be related to one another, at the very least indirectly. For example, let us assume one were to describe the structure of an atomic nucleus with a self-consistent mean-field model based on some effective nucleon-nucleon potential [28]. How this mean field is computed or parametrized should directly impact the optical potential (the real part of the optical potential does represent the nuclear mean field); the nuclear level density (through the excited states associated with the mean-field potential); the gamma-strength-function (which is typically related to functional derivatives of the mean field with respect to nuclear densities); fission transmission coefficients (which depend on how the mean-field potential changes with deformation), etc. Moreover, since the same effective nucleon-nucleon potential would be used to compute every single nucleus, nuclear properties would also be heavily correlated as a function of proton and neutron number.

Therefore, even if such a theoretical model still contains parameters fitted to experimental data – in this case: the parameters of the effective nucleon-nucleon force, all nuclear properties are directly related to that single set of parameters. In a sensitivity analysis, one would find that variations of the model parameters result in *correlated* variations of the model outputs, i.e., the nuclear data properties of interest. In current approaches based on separate models for each type of nuclear data, such correlated variations, which manifest relationships between different data, are impossible to capture with nuclear theory alone.

Instead, each nuclear model is treated as a separate black box independently parametrized by a handful of parameters. In a typical evaluation process, these parameters are adjusted in such a way that nuclear cross sections match experimental measurements and the resulting benchmarks are satisfied [2–4, 29]. These fits will often take the form of a functional dependency of model parameters in terms of proton and neutron number (or atomic mass number A), excitation energy or angular momentum. The nuclear reaction codes mentioned above typically implement a few different variants of such systematics. By construction, these systematics become highly questionable in nuclei or at energies that are beyond the range of their fit, which directly impacts the reliability of nuclear data libraries in these regions.

By employing a collection of independent nuclear models locally calibrated to experimental data, it thus be-

comes nearly impossible to (1) make reliable predictions outside the range of currently available measurements (2) capture the relationships (or correlations) between nuclear data within the same nucleus, or between different nuclei. In this paper, we will show that deep-learning techniques provide an alternative solution to point (2) .

III. METHODOLOGY

The limited number of available data for individual cross sections together with the potentially complex relationships between cross sections of different nuclei can make the training of deep learning models challenging. To overcome such a challenge, we separate the overall learning problem into two interconnected components, namely a representation learning task and a prediction task, as shown in Fig. 1. In the representation learning task, we are learning the low-dimensional, latent space representation of cross sections; in the prediction task, we make predictions to unknown nuclei from such latent representations and use the decoder trained in the first task to bring them back into the original space of cross sections. In contrast to the space of cross sections, the latent space provides a more compact yet meaningful representation that allows the model to learn more rapidly and generalize better. Additionally, the separation of these two steps ensures a clear delineation between the process of learning the representation, which may require data augmentation, i.e., interpolation and scaling of the cross-section data, and the actual prediction tasks, which should only involve the cross section data that physically exist, i.e., a cross section that is not augmented with additional, synthetic data or modified.

As schematically illustrated in Fig. 1(a), the representation learning component will focus on learning the underlying latent representation space of all known cross sections. In the following discussion, we note $\sigma_\alpha(E)$ the cross section of the nuclear reaction, or channel, α as a function of the energy E of the incident particle, where the energy is discretized on a finite grid $E \rightarrow \{E_o\}_{o=1,m}$, where m is the dimension of the original data vector. For the encoding of the cross-section, we train either a 1D-convolutional VAE [30] or an encoding-decoding hypernetwork [31] that predicts the weights for the INR model [32] on data from s nuclei to learn a k -dimensional latent space for various cross sections. By design, $k < m$ so that the size of the feature matrix is reduced to $\mathbf{X} \in \mathbb{R}^{s \times k}$ while keeping the implicit grid intact.

For the prediction task shown in Fig. 1(b), we rely on a GNN approach. The available cross section data in the latent space can be represented as a graph $\mathcal{G} = (\mathcal{V}, \mathcal{E})$, where each nucleus is represented by a node $v_i \in \mathcal{V}$ (the set of total nodes) while the relationship between nodes v_i, v_j constitutes an edge $e_{ij} \in \mathcal{E}$ (the set of edges). Each node v_i with $i \in [0, s - 1]$ consists of a k -dimensional feature vector \mathbf{x}_i , defining the feature matrix $\mathbf{X} \in \mathbb{R}^{s \times k}$.

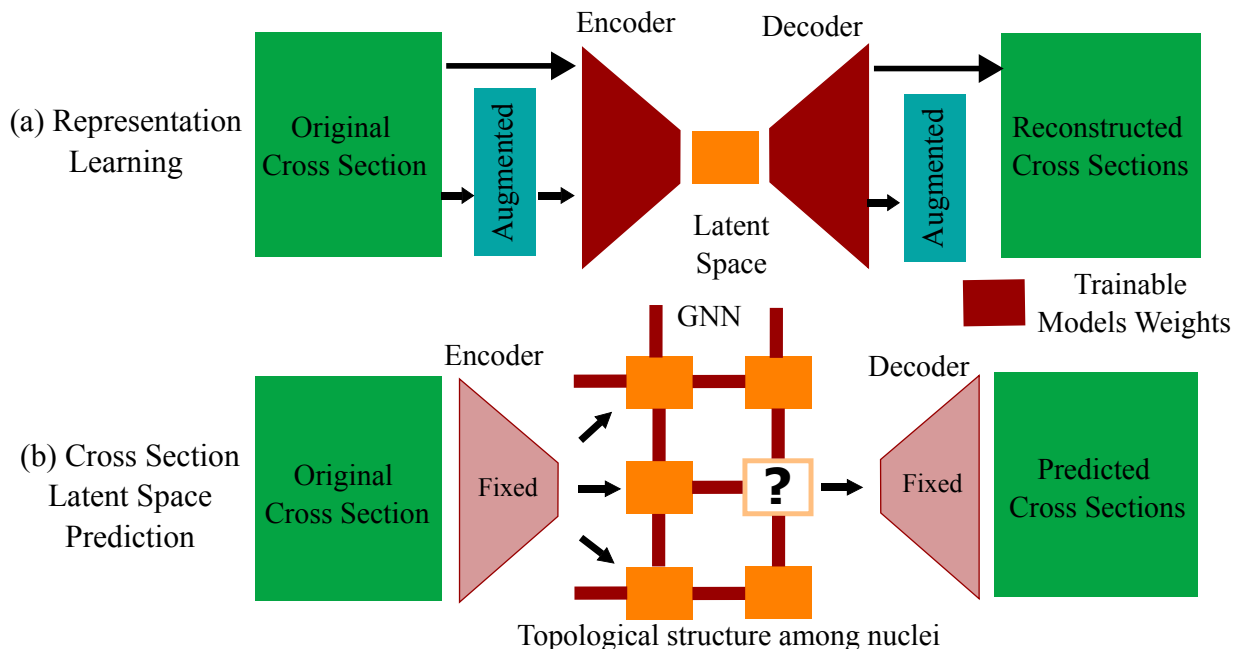


Figure 1. Schematic representation of our framework. The initial data is a (set of) nuclear cross sections represented as a vector indexed by the energy of the incident particle. The data is encoded into a latent representation using either a variational autoencoder (VAE) or an implicit neural representation (INR) network (representation learning). A graph neural network (GNN) then learns how the data in the latent space in nucleus (Z, N) transforms into neighboring nuclei in order to make predictions in nucleus (Z', N') . The decoder then transforms the predicted vector in the latent space back into the space of nuclear cross sections (latent space predictions).

A. Dataset

Our dataset is a subset of the TENDL dataset of nuclear cross sections [29]. In practice, we only consider the (n, el) (i.e., elastic), (n, n') (i.e., inelastic), (n, γ) and $(n, 2n)$ cross sections for all nuclei included in TENDL. Since cross sections are probabilities per unit area, their values are always positive: $\sigma_\alpha(E) \geq 0$ for all channels α . The TENDL dataset contains $s = 2151$ nuclei and can be represented in a 2D grid corresponding to the chart of isotopes and labeled as (N, Z) with N the neutron number and Z the proton number of the nucleus. For the elastic, inelastic, (n, γ) and $(n, 2n)$ channels the original cross section is defined on an energy grid of $m = 256$ points regularly spaced between 0 and 20 MeV. The values of each type of cross section are normalized by dividing by their maximum across the dataset. As discussed before, the data is then embedded into a lower k -dimensional latent space with $k = 32$ using either a pre-trained VAE or INR model, resulting in a final data matrix of size $(s \times k) = (2151 \times 32)$.

The size of the TENDL dataset is rather small to train deep learning models such as VAEs or INRs. This can be mitigated using data augmentation techniques. In the representation learning task, we only focus on the cross section data, i.e., describing curves, rather than any underlying physical relationship and properties. The goal is simply to construct a continuous, multi-dimensional

latent space of curve shapes. Since we do not directly assign any physical properties to such a space, we can adopt an interpolation-based data augmentation strategy, in which we produce new training examples by linearly interpolating between two randomly picked cross section samples with weights that add up to 1.0. Essentially the latent space thus generated provides a super-set of all valid cross-sections while at the same time allowing for a smooth transition between them for better optimization in the cross-section prediction task with the GNN. For the latter, only actual cross sections in existing nuclei are used as training data.

B. Representation Learning

Representation learning aims to condense raw input data into a concise format, preserving crucial information for target tasks. Ideally, the learned representation provides a lower-dimensional space which makes subsequent learning tasks more efficient. In our setup, the goal of representation learning is to learn the space of all cross sections. By doing so, not only can all known cross sections of a nucleus be encoded in the representation space, we can also predict new cross sections for known and unknown nuclei. This prediction task then just translates into the task of finding the right vector in the learned representation space.

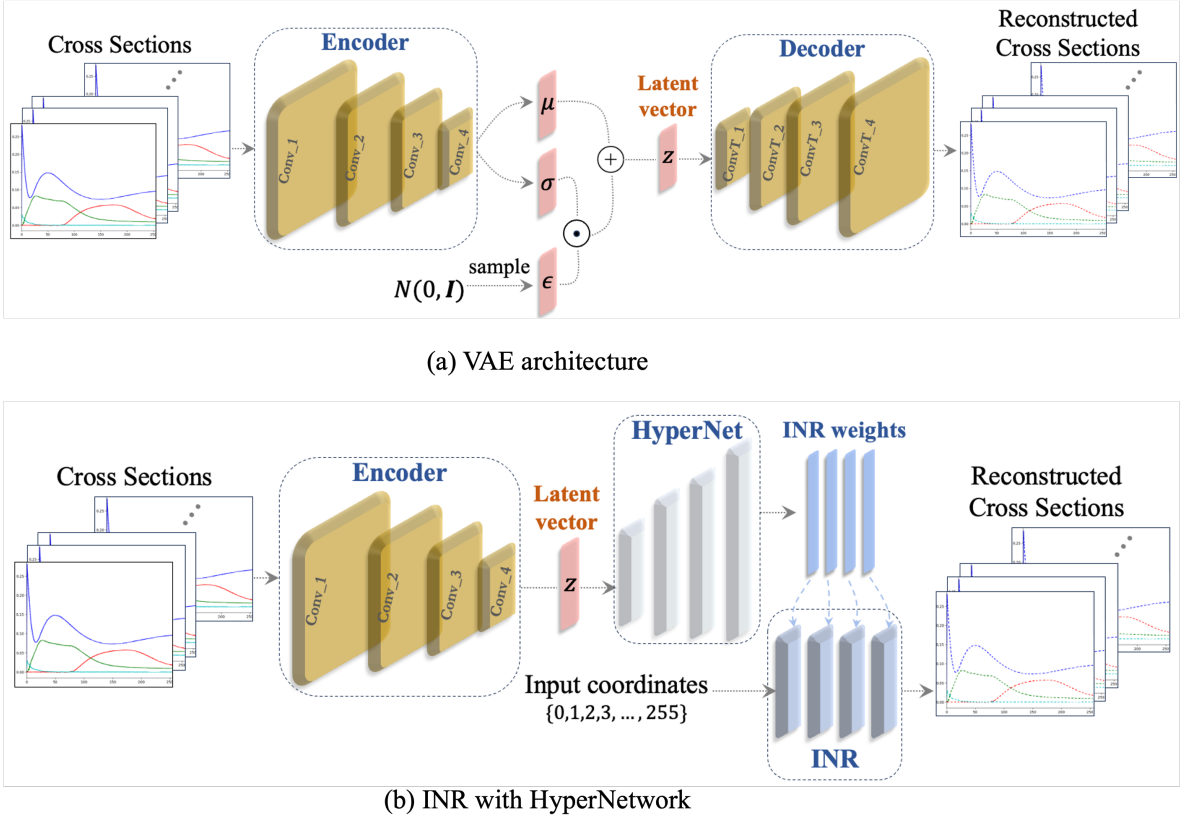


Figure 2. (a) Variational Autoencoder framework illustrating the encoding and decoding process with a latent space bottleneck. (b) Implicit Neural Representation (INR) architecture integrated with a hypernetwork (HyperNet). The hypernetwork generates weights for the INR, informed by a convolutional encoder that processes input data. Note that the INR takes input coordinates (representing the energy index with a length of 256) and maps them to the corresponding cross-sections.

1. Variational Autoencoder

One of the most commonly used approaches for representation learning is an autoencoder (AE) architecture. An AE is a neural network designed to encode input data into a lower-dimensional space (i.e., bottleneck) and then decode it back to the original data space. As illustrated in Fig. 2(a), the autoencoding objective is centered around minimizing the discrepancy between the original input and the reconstructed output. For variational autoencoders (VAEs) [25], the standard autoencoding objective is augmented by the inclusion of variational inference [33], where the encoding process maps input data not to a fixed point but to a probability distribution in the latent space. This dual training objective involves both minimizing the reconstruction error and aligning the latent space distribution with a specified form, i.e., a standard Gaussian distribution (with parameter σ and μ). Specifically, the VAE training loss can be defined by two key terms, the reconstruction loss and the Kullback-Leibler (KL) divergence,

$$\mathcal{L}_{\text{VAE}} = -\mathbb{E}_{q_{\phi}(z|x)}[\log p_{\theta}(x|z)] + \lambda \cdot D_{\text{KL}}(q_{\phi}(z|x)||p(z)) \quad (1)$$

The first term encourages the VAE to accurately reconstruct the original input data. It measures the negative log-likelihood of the decoder distribution ($p_{\theta}(x|z)$) generating data that resembles the input (x) given a sampled latent code (z) from the encoder distribution ($q_{\phi}(z|x)$). The second term acts as a regularizer, forcing the learned latent distribution ($q_{\phi}(z|x)$) to be similar to a prior distribution ($p(z)$), i.e., a standard normal Gaussian. The hyperparameter λ controls the balance between reconstruction accuracy and the regularity of the latent space. Following the original VAE formulation, we set λ to 1.

The integration of variational inference ensures a continuous representation space and makes the network generative: we can generate diverse and realistic new data simply by sampling from the learned latent space distribution and applying the decoder. Overall, VAEs provide a powerful framework for unsupervised representation learning, while at the same time facilitating high-quality reconstruction and generation.

In this work, the encoder of the VAE model comprises a sequence of convolutional layers followed by ReLU activation functions [34] and a flattening operation. This architecture is designed to progressively reduce the spatial dimensions of the inputs while increasing the number

of feature channels. Our encoder includes four convolutional layers – noted conv_1, conv_2, conv_3, and conv_4 in Fig. 2 – with increasing filters (32, 64, 128, 256), kernel size 4, and stride 2. Each layer is followed by a ReLU activation. We then convert the output of convolutional layers into a flattened vector of size k .

The decoder comprises a sequence of transposed convolutional layers aimed at reconstructing the original inputs from the latent space. It also employs ReLU activations and concludes with a sigmoid activation for the reconstructed inputs. As the mirror opposite of the encoder, the decoder progressively refines the representation through four layers with specific filter sizes and strides: 128 filters with a kernel size of 5 and stride of 2, followed by 64 filters with a kernel size of 5 and stride of 2, then 32 filters with a kernel size of 6 and stride of 2, and finally, the output layer with a kernel size of 24 and a stride of 8. The output layer returns a vector of size m . By jointly optimizing the encoder and decoder, the VAE learns a compact and informative representation of given inputs.

2. Implicit Neural Representation

INR is a method for representing and modeling input data without explicitly defining the geometry or structure of objects [32, 35]. Traditional data encoding methods rely on discrete representations, such as data grids, which are constrained by their spatial resolution and are susceptible to inherent discretization artifacts. In contrast, INR represents input data (including sound, time-series, images, and 3D scenes) as a continuous function of its coordinate locations, where each value is generated independently. This function is approximated by a deep neural network. INR offers flexibility and adaptability for encoding data independent of resolution through the use of coordinate grids, making them highly effective with numerous potential applications [35–37].

While INRs offer advantages in practical scenarios, they face the limitation of often struggling to generalize beyond the single input on which they were trained. This can hinder their effectiveness in deep learning applications, where robust generalization across diverse training datasets is crucial. To address this issue, hypernetworks have been introduced [31]. Hypernetworks act as meta neural networks, generating weights for a primary neural network, the desired INR. Sitzmann et al. [32] successfully employed a convolutional encoder and hypernetwork combination to guide the INR in learning more generalizable representations of training data. This unified framework helps the INR overcome the ‘single-fit’ limitation by learning priors over the input space, enhancing its representational capabilities while maintaining its accurate reconstruction abilities.

As shown in Fig. 2(b), our framework integrates a hypernetwork with an INR. The convolutional encoder leverages the same configuration as in Fig. 2(a), featuring

a series of convolutional layers. It processes cross-section data and compresses it into a 32-dimensional latent vector. This vector is then passed to the hypernetwork decoder, which consists of standard multi-layer perceptron layers with ReLU activations. The hypernetwork’s output provides the weights for the INR. Finally, the INR takes coordinates as input and reconstructs the original input data. This pipeline enables networks to be trained in an end-to-end manner by minimizing the following loss function

$$\mathcal{L}_{\text{INR}} = \mathcal{L}_{\text{recon}} + \alpha \mathcal{L}_{\text{latent}} + \beta \mathcal{L}_{\text{weights}}, \quad (2)$$

where $\mathcal{L}_{\text{recon}}$, $\mathcal{L}_{\text{latent}}$, and $\mathcal{L}_{\text{weights}}$ represent the reconstruction loss, regularization terms for latent vectors and weights in the hypernetwork. The hyperparameters α and β are utilized to balance the contributions of the different losses. Specifically, each loss term is computed as follows:

$$\mathcal{L}_{\text{recon}} = \frac{1}{N_{\text{batch}}} \sum_{i=1}^{N_{\text{batch}}} \|\mathbf{y}_i - \hat{\mathbf{x}}_i\|_2, \quad (3a)$$

$$\mathcal{L}_{\text{latent}} = \frac{1}{N_{\text{batch}}} \sum_{i=1}^{N_{\text{batch}}} \|\mathbf{z}_i\|_2^2, \quad (3b)$$

$$\mathcal{L}_{\text{weights}} = \frac{1}{N_{\text{batch}}} \frac{1}{N_{\mathcal{W}}} \sum_{i=1}^{N_{\text{batch}}} \sum_{\mathbf{w} \in \mathcal{W}} \|\mathbf{w}_i\|_2^2, \quad (3c)$$

where $\|\dots\|_2$ is the usual Euclidean norm. Here, \mathbf{y}_i represents the i -th ground truth input and $\hat{\mathbf{x}}_i$ its corresponding reconstruction. N_{batch} represents the batch size, indicating the number of samples processed during each training iteration. \mathbf{z}_i refers to the latent vector with k dimensions produced by the encoder for the i -th sample in the batch. $N_{\mathcal{W}}$ represents the total number of parameters in the INR model, and \mathbf{w}_i are the individual weights. Note that $\mathcal{L}_{\text{latent}}$ and $\mathcal{L}_{\text{weights}}$ are regularization terms that aim to decrease the overall magnitude of feature and weight representations, making them less prone to overfitting by penalizing large magnitude. Through empirical evaluation, we determined that setting $\alpha = 0.01$ and $\beta = 1.0$ results in optimal reconstruction performance.

C. Graph Neural Networks

GNNs are optimizable transforms that operate on all attributes of a graph (nodes, edges, global context, inherent relationships, etc.) while preserving symmetries and the underlying structure of the data. This lends to their excellent capabilities to estimate non-Euclidian subspaces and hence, GNNs are ideal for this case where we seek to expose and explore the relationships between nuclear cross-sections across a two-dimensional grid. GNNs accept a graph as input (the encoded 2D TENDL grid) with the information contained in the nodes (feature vectors) and perform transformations without changing the

connectivity of the input. GNNs also produce a graph at the output.

The graph $\mathcal{G} = (\mathcal{V}, \mathcal{E})$ is created using the encoded data obtained from the encoding module of the representation learning architecture (VAE or INR) with a mask imposed on the test set so that it is not visible during training. For optimization, we calculate the loss as

$$\mathcal{L}_{\text{GNN}} = \|\chi(\mathcal{G}) - \mathbf{y}_z\|_2, \quad (4)$$

where \mathcal{G} is the input graph to the GNN, χ is the chosen GNN architecture, and \mathbf{y}_z is the encoded cross section representation from the TENDL library, i.e. the encoded ground truth. The loss optimization is performed in the latent space to ensure better convergence characteristics and to leverage the excellent performance of the representation learning module; see Fig. 3.

In this work, GNNs are constructed using the ‘‘message passing neural network’’ (MPNN) backbone [38]. MPNNs follow an iterative scheme to update the nodes by aggregating information from other nearby nodes. The aggregation function is permutation invariant and passes on the aggregated information to the next layer. For the regular grid graph considered in this paper, the forward pass through the GNN has two phases – a message passing phase and a readout phase. In the message passing phase for a particular node, the message function M_t aggregates the information from its neighbors and updates the node according to some update function U_t . At any time t , the hidden state h_i^t at node v_i is updated as

$$m_i^{t+1} = \sum_{j \in N(v_i)} M_t(h_i^t, h_j^t, e_{ij}), \quad (5)$$

$$h_i^{t+1} = U_t(h_i^t, m_i^{t+1}), \quad (6)$$

where $N(v_i)$ denotes the neighbors of node v_i in the graph \mathcal{G} . Here, neighbors are defined by the adjacency to the original node: the neighbors of v_i are all the nodes that are next to it in the (Z, N) grid. The readout phase computes a feature vector for the whole graph using some readout function R_t . M_t , U_t , and R_t are all learnable differentiable functions that are separately estimated using machine learning methods.

We construct three different GNN architectures based on ARMAConv [39], GatedConv [40], and the traditional GCN (Graph Convolution Network) [41] with the goal of establishing a performance baseline for this data type. The traditional GCN employs a convolution layer that operates on the input feature matrix \mathbf{X} , with the adjacency matrix \mathbf{A} , a degree matrix \mathbf{D} , and filter parameters Θ in the Fourier domain. The positional relationships (edge e_{ij} between any two input nodes v_i, v_j) of the input data are captured by \mathbf{A} . In contrast, GatedConv is designed for sequence prediction using the recurrence of the basic graph propagation model where a sequence of node annotations \mathcal{X} and node state machines \mathcal{H} are used to produce an output sequence. Finally, ARMAConv experiments explore the effect of auto-regressive filter layers instead of the traditional polynomial spectral filters.

This layer can model complex relationships with fewer parameters and learns a representation independent of the underlying graph architecture. The initial node features \mathbf{X} are transformed using learnable parameters \mathbf{W} and \mathbf{V} , the original Laplacian of the graph, \mathbf{L} , and some non-linearity $\sigma(\cdot)$ such as ReLU. All these architectures considered use the MPNN backbone with slight variations either in terms of the type of filter used or the node update method.

IV. RESULTS

We recall that our proposed framework consists of two main components. In a first step, we learn the latent vector encoding the nuclear cross sections with dimensionality reduction techniques. In a second step, we train a GNN to predict the latent vector in neighboring nuclei by leveraging the learned latent vector before the decoder transforms the data back to the original 256-dimension cross-section. Since a crucial part of dealing with GNNs is the lower-dimension representation space, we first analyze our two encoding mechanisms – the VAE model of Fig. 2(a) and the INR model of Fig. 2(b). We then present the results of several experiments designed to study the behavior of different GNN architectures. Specifically our goal is to infer unknown (i.e., test set) cross-sections based on the knowledge learned from the known cross-sections in the training set.

A. Encoding Performance

The quality of the latent representation plays a critical role to predict accurate cross sections. Therefore, in this section we focus on evaluating the quality of the latent space learned by both the VAE and INR.

For this experiment, we randomly split the dataset containing 2151 samples into a training set ($\approx 90\%$) and a testing set ($\approx 10\%$). To ensure reproducibility and fair comparisons, we employed a fixed random seed, guaranteeing both models were trained on identical datasets. Prior to model training, we normalized the input data by dividing each cross-section by its corresponding maximum value across the entire dataset. This ensures that each cross-section falls within the range of $[0, 1]$. Then, the VAE model was trained on a multi-channel cross-section dataset for 5,000 epochs with a batch size of 32. We utilized the Adam optimizer (initial learning rate 1×10^{-3}) for optimization. The INR model, trained on the same dataset, also used the Adam optimizer (learning rate 5×10^{-5}) but for 600 epochs. Notably, the INR model demonstrated significantly faster convergence compared to the VAE training while maintaining high quality of latent representations.

Figure 3 illustrates the typical performance of both the VAE (top) and INR (bottom) for a nucleus within the TENDL dataset. Each color represents one of the

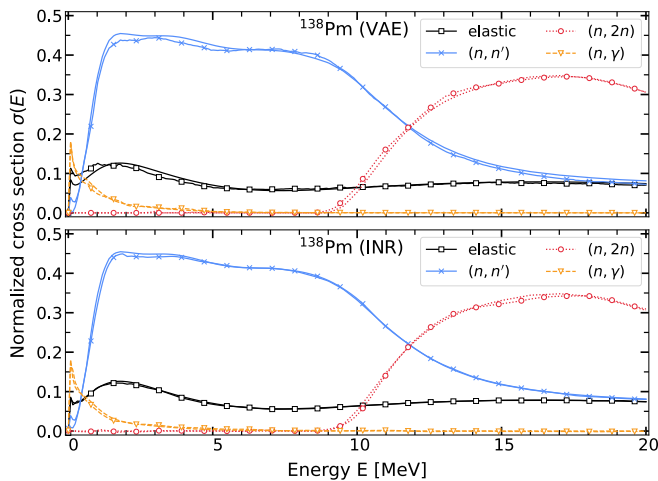


Figure 3. Comparison of the encoding performance between VAE (top) and INR (bottom) for all four cross sections in the ^{138}Pm nucleus. Ground-truth results are shown in plain lines and full symbols while reconstructions are in dashed lines and open symbols. Performance is typical of all nuclei in the TENDL dataset.

four cross-section channels considered in this work. The curves with symbols (square, circle, x, inverted triangle) represent the reconstructed inputs generated by either the VAE or the INR, whereas plain curves depict the ground truth inputs. As seen in this figure, both models effectively reconstruct given test samples, closely aligning with the ground truth. These results demonstrate that both models are able to encode the multi-channel cross-section input into a compact, 32-dimensional latent vector with minimal loss in reconstruction accuracy.

To quantify reconstruction performance, we adopt the Peak Signal-to-Noise Ratio (PSNR). The PSNR is defined as follows:

$$\text{PSNR} = 20 \log_{10} \left(\frac{\text{MAX}}{\sqrt{\text{MSE}}} \right), \quad (7)$$

where $\text{MSE} = \frac{1}{n} \sum_{i=1}^n \|\mathbf{y}_i - \hat{\mathbf{x}}_i\|_2^2$, $\hat{\mathbf{x}}_i$ represents the reconstructed input generated by either the VAE or the INR, while \mathbf{y}_i denotes the original cross-sectional inputs. Here, n is the total number of testing samples. MAX represents the maximum possible value of the signal, which is equal to 1. We evaluate each model using this metric on the entire test set. The VAE achieves a score of 43.67, while the INR achieves a higher score of 47.20. Overall, the performance of the INR is significantly better as this model is better able to precisely capture high-frequency information such as thresholds, for example the fact that the cross section for the $(n, 2n)$ cross section is identically 0 unless the energy of the incident neutron exceeds the neutron separation energy. For completeness, Appendix VII A shows the evolution of the train and test losses as well of the train and test PSNR as a function of epochs.

B. GNN performance

The training of the GNN requires a partitioning of the TENDL dataset that is different from the one adopted in the training of the VAE and INR. Since the goal of the GNN, after training, is to make predictions of cross sections, possibly a few neutrons away from the training set, we divide the entire TENDL dataset into a training and test set based on a windowing function. The windowed test set is created using a rectangular window centered around a specific nucleus (Z_0, N_0) in the chart of isotope and containing all nuclei with $Z_0 - \Delta Z \leq Z_0 \leq Z_0 + \Delta Z$ and $N_0 - \Delta N \leq N_0 \leq N_0 + \Delta N$. All results presented in this section were obtained for a test window centered on $(Z_0, N_0) = (42, 60)$ with $\Delta Z = \Delta N = 8$. This window contains a total of 289 test nuclei, 209 of which are included in the original TENDL dataset. Since that original dataset contains 2151 points on the 2D plane, this means that about 7.2% of the total data is allocated to the test set. Appendix VII B gives results obtained with different window center locations and different window sizes.

All of the GNN models are trained for 5000 epochs with a learning rate of 1×10^{-3} on the training data. We use an Adam optimizer [42] with $\beta_1 = 0.9, \beta_2 = 0.999$. For each epoch, the entire training set is passed through the GNN and we do not create batches of the training graph since breaking the edge relationships between the nodes would yield inaccurate results. The prediction error of the decoded cross-sections is computed as

$$\epsilon = \frac{1}{n} \sum_{i=1}^n \|\mathbf{y}_i - \hat{\mathbf{x}}_i\|_2^2, \quad (8)$$

where $\hat{\mathbf{x}}_i$ and \mathbf{y}_i are the predicted node features and the ground truth in the original space, respectively, and n is the actual number of nuclei in the set (either training or test). The quantity $(\mathbf{y}_i - \hat{\mathbf{x}}_i)$ computes the point-wise difference and is a 256-dimension vector, which is then summed for each position i in the test set. In the training phase $n = 1942$ (the 2151 original nuclei of the TENDL dataset minus the 209 of the test window). During inference, the trained GNN is used to predict the node features in the test set and $n = 209$. Since the model was only trained on the training data, there is no contamination bias from the test set on the GNN. The predicted cross-sections are then decoded using the chosen decoder \mathcal{D} , which is kept frozen to prevent any updates to the weights. We calculate the prediction error in the 256-dimension space using Eq. (8) and report it in Fig. 4 and Fig. 5.

In Fig. 4, the overall spread of the error is presented for all points in the dataset. We theorize that the traditional GCN architecture is too simple to estimate the structure of the TENDL grid. This is validated by the plots in Fig. 4 (bottom row), where the spread of the error in the GCN is quite large. On the other hand, the ARMA model shows excellent predictive performance in the test set for

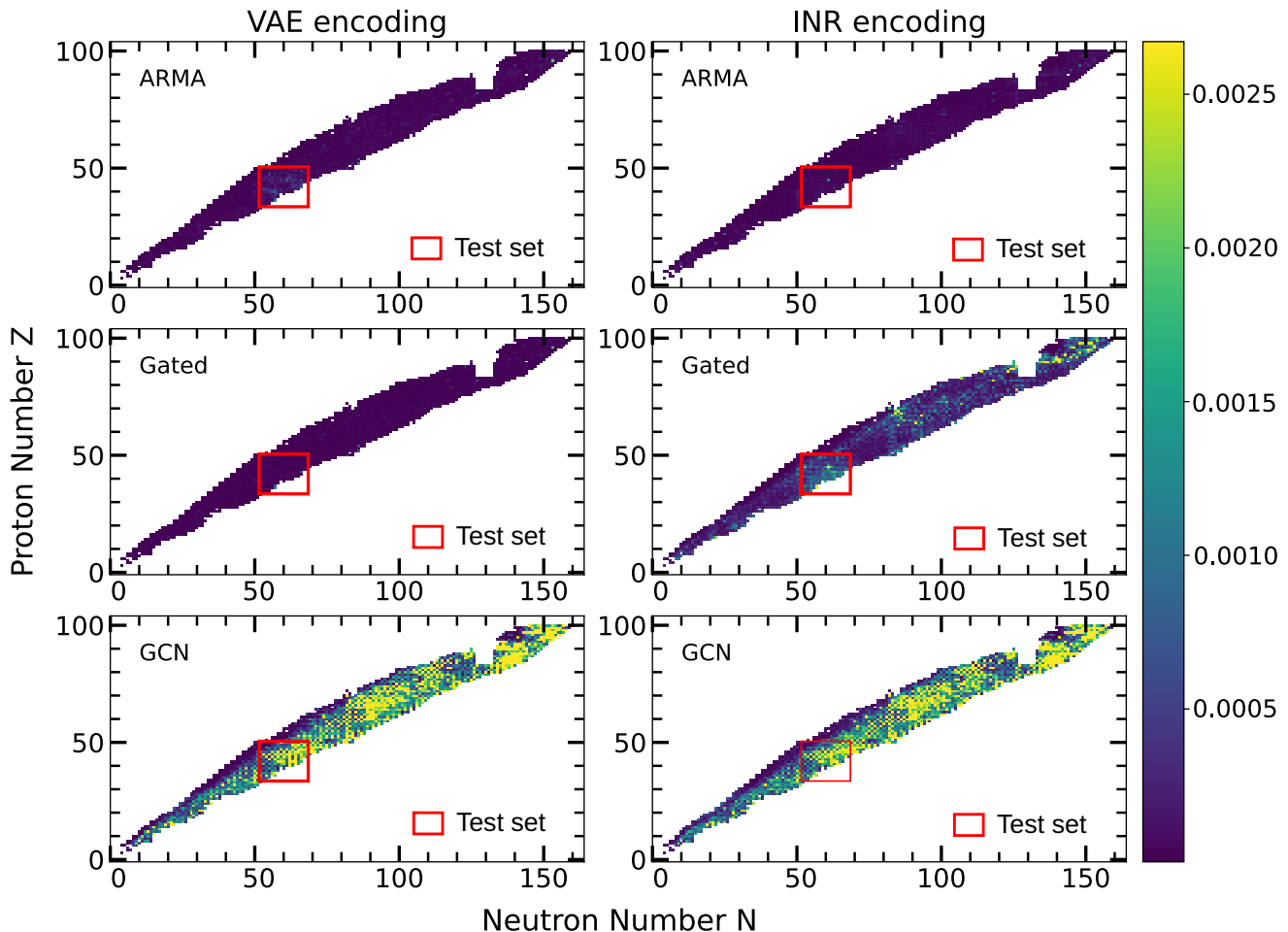


Figure 4. Mean prediction errors calculated using Eq. (8) of the GNN for each nucleus in the TENDL dataset. For better visualization, all plots are normalized between ϵ_{\min} and $0.1 \times \epsilon_{\max}$, where ϵ_{\min} (ϵ_{\max}) is the minimum (maximum) error over all plots. The three panels on the left side are based on VAE encoding while the three on the right on INR encoding. ARMA, Gated and GCN refer to the three types of GNNs considered in this work. The red square corresponds to the windowed test data: the GNN was not trained on it.

both the VAE and INR encoding. Interestingly, while the GatedConv model behaves as expected for the VAE encoding, we observe that for the case of the INR, there is a drop in performance. As we will discuss in Section V, this is a consequence of the fact that the INR latent space is more restricted than the one from the VAE.

Since the GNN seeks to estimate the latent manifold to learn the underlying relationships of the graph, a narrow distribution of the latent variables hinders the GNN from learning these relationships accurately. To better quantitatively measure the performance of each network, we list in Table I the average test PSNR using Eq. (7) over all points in the test set. We also provide comparisons with and without interpolation-based data augmentation, denoted as DA in the table.

To better visualize the performance of each network in the prediction task, we show in Fig. 5 the normalized cross sections in three different nuclei within the test window: ^{86}Se is at the “lower left” corner of the window;

Table I. Test PSNR values of the different GNN architectures with and without data augmentation (DA).

	ARMA	Gated	GCN
VAE (DA)	37.80	43.46	27.75
VAE (no DA)	37.47	43.44	27.80
INR (DA)	42.23	31.80	27.99
INR (no DA)	42.98	31.63	28.10

^{102}Mo is exactly at the center (hence the furthest away from the training set); ^{118}Sn is at the “upper right” of the window. For each nucleus, we look at the performance of the GNN depending on whether the encoding was from a VAE or an INR. According to Table I, the best GNN architecture with VAE encoding is GatedConv while it is ARMAConv for the INR encoding. For each encoding, the figure shows the results for the optimal GNN architecture. In the case of the VAE, the predictive power is

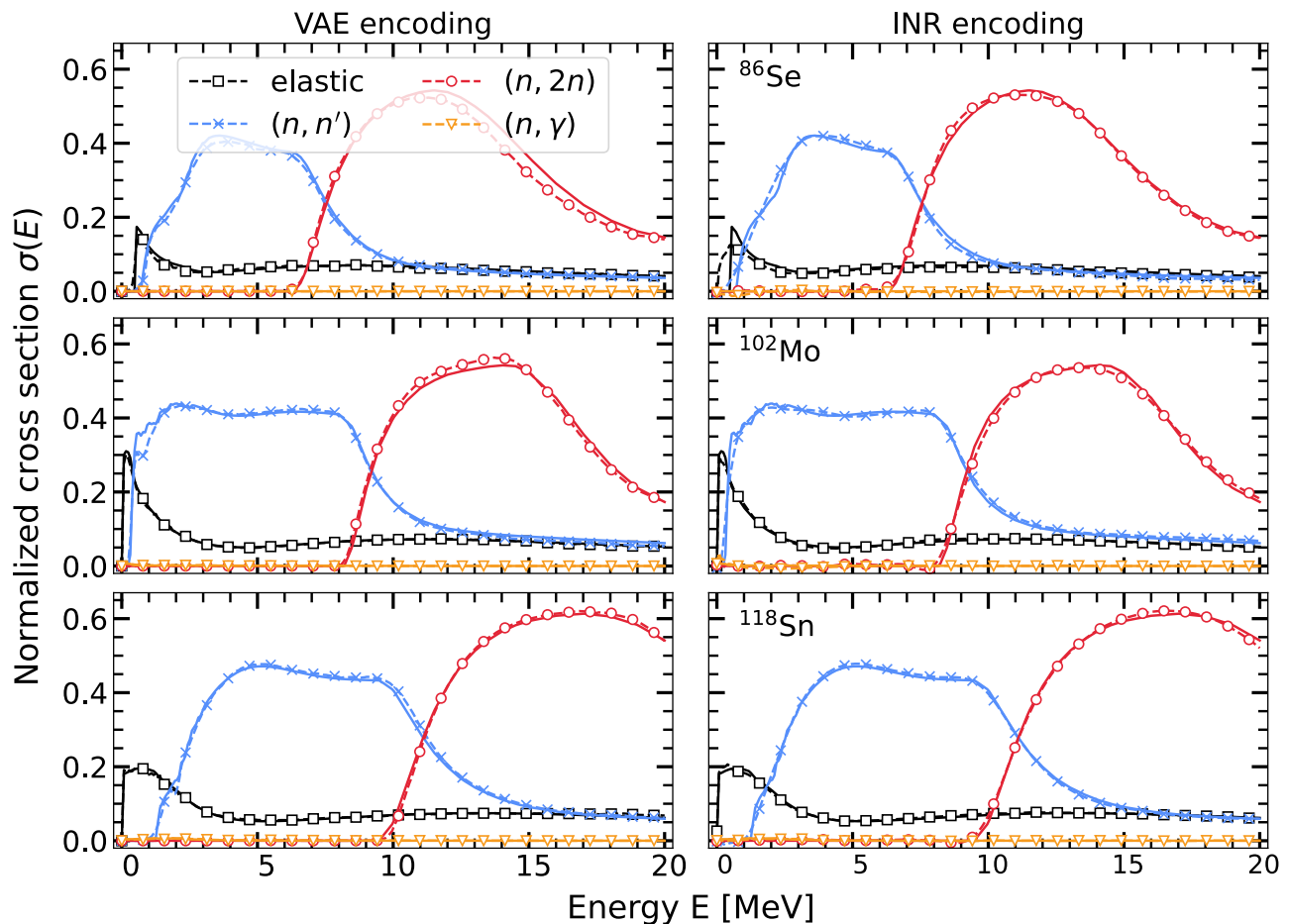


Figure 5. Performance of the VAE and INR model for the GatedConv(left) and ARMAConv (right) GNN architecture in predicting nuclear cross-sections within the test set for the central nucleus, ^{102}Mo and the ones at the lower left and upper right of the window, ^{86}Se and ^{118}Sn respectively. Plain curves without symbols correspond to the ground truth while dashed curves with open symbols correspond to GNN predictions. All cross sections are normalized independently in each channel across the entire dataset.

rather good since most of the curves are hardly distinguishable, the exception being the $(n, 2n)$ cross section in ^{86}Se . The performance of ARMAConv with the INR encoding is visibly improved compared to that of the VAE, as reaffirmed by the values in Table I. Note that the (n, γ) channels is not identically zero but the normalized cross section is several order smaller than the other ones for these particular nuclei.

V. DISCUSSION

The results presented in Section IV pose a few interesting questions, both from a data science and from a nuclear physics perspective, which we discuss in this section. In particular, we focus on a brief analysis of the structure of the latent space to analyze if specific patterns can be matched to nuclear properties. We also outline how our framework lends itself to propagating uncertainties of cross sections throughout the nuclear chart.

A. Representation learning and structure of the latent space

First, we emphasize the importance of the training objective of Eq. (4) for successful GNN training. When training the GNN with the original cross-sections as targets (i.e., $\mathcal{L}_{\text{GNN}} = \|\mathcal{D}(\chi(\mathcal{G})) - \mathbf{y}\|_2$), where \mathcal{D} represents the VAE or INR decoder, and \mathbf{y} is the original cross-sections with 256 dimensions, we observe that the GNN prediction performance is degraded with INR-based encoding compared to VAE. Unlike VAEs, which promote continuous representations through regularization (e.g., standard normal Gaussian prior), the INR's latent space is more tightly constrained by its regularization term, particularly $\mathcal{L}_{\text{latent}}$. This restriction may suppress features that would be discriminative for downstream prediction tasks. Additionally, the INR's interconnected decoder architecture, where a hypernetwork generates the INR's weights, could amplify the impact of perturbations in INR weights during GNN training, further hindering prediction performance.

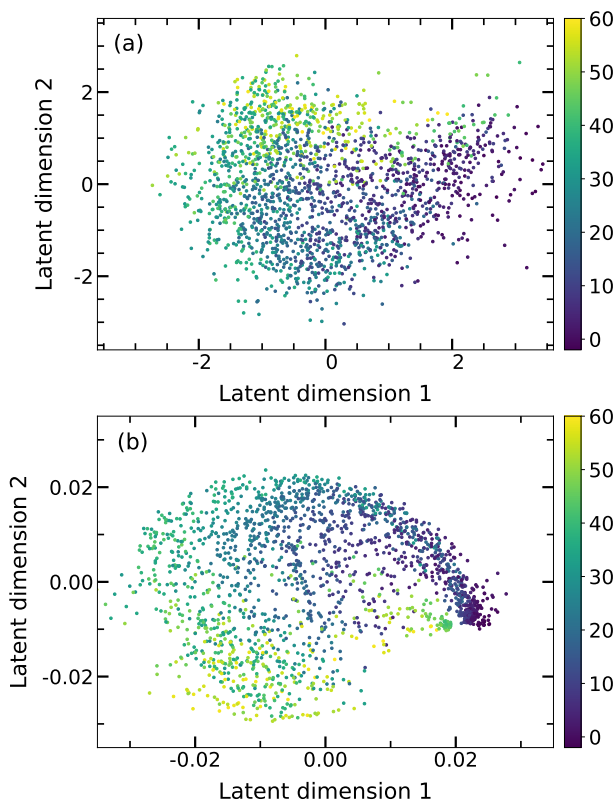


Figure 6. PCA visualization of the VAE and INR hypernet latent spaces. Panel (a): projections of each k -dimensional VAE latent vector onto a two-dimensional plane spanned by the two largest components of the PCA. Panel (b): same figure for the INR latent vector.

In Fig. 6, we show a direct visualization of the latent spaces for the training dataset of both the VAE and INR models. In both panels, we perform a principal component analysis (PCA) of the k -dimensional latent vectors ($k = 32$) and project each of them onto the two-dimensional plane spanned by the two largest PCA components. Panel (a) corresponds to the VAE latent space while panel (b) corresponds to the INR latent space. We recall that each point in such a figure corresponds to a given nucleus; its color is the value of the difference $N - Z$ of the neutron number N and proton number Z in the corresponding nucleus. The only noticeable difference is that the samples’ variability scale for the latent space in the INR model is significantly smaller than for its VAE counterpart: the INR hypernet latent space is much more “compact” than the VAE one.

To better understand the structural differences between the two encoding techniques, we compute the t-distributed stochastic neighbor (t-SNE) embedding [43]. Let us quickly recall the basics of the t-SNE method. Assume we have a set \mathcal{P} of points P in a n_p -dimensional space, and characterize the “similarity” of two points P and P' in \mathcal{P} by some joint probability distribution function p . Let us now assume that \mathcal{P} can be mapped onto

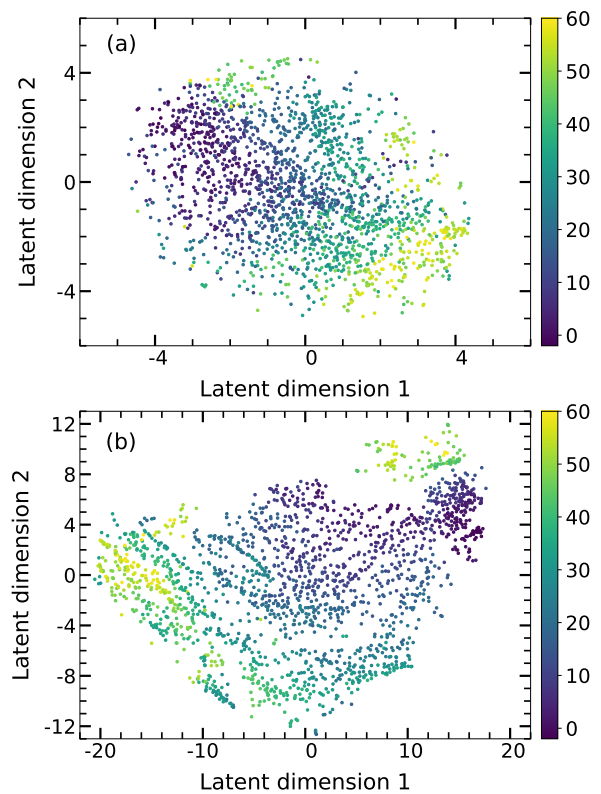


Figure 7. t-SNE visualization of the VAE and INR hypernet latent spaces. Panel (a): two-dimensional t-SNE embedding of k -dimensional VAE latent vectors obtained for a perplexity value of 200. Panel (b): same figure for the INR latent vector.

a set \mathcal{Q} of points Q in a n_q -dimensional space ($n_q \ll n_p$) that is characterized by another probability distribution q . The t-SNE technique minimizes the Kullback-Leibler divergence \mathcal{L}_{PQ} between the joint probabilities p in the high-dimensional space and the joint probabilities q in the low-dimensional space. In simple terms: two points that are “neighbors” in the high-dimensional space should also be neighbors in the low-dimensional one.

Figure 7 shows the two-dimensional representation of this t-SNE embedding for both the VAE and INR encodings as obtained with the `scikit-learn` implementation. Like Fig. 6, the color of a point is the difference $N - Z$ of the neutron number N and proton number Z in the corresponding nucleus. In practice, t-SNE algorithms require setting a few hyperparameters, most notably one called “perplexity” Perp which can be interpreted as “a smooth measure of the effective number of neighbors” in the high-dimensional space [43]. Although traditional implementations of t-SNE suggest values of the perplexity between 5 and 50, this is highly dependent on the dataset and its dimensionality. In our case, the dataset has 1936 points – training nuclei represent 90% of the whole TENDL dataset of 2151 nuclei – and is encoded in a latent space of dimension $k = 32$. We found that in order to converge the Kullback-Leibler loss \mathcal{L}_{PQ} ,

the perplexity parameter had to be significantly larger: figure 7 was obtained for $\text{Perp} = 200$. Note that the spatial arrangement of points and the variability scale in each latent dimension are very dependent on the value of Perp . In particular, small values of Perp (corresponding to large values of \mathcal{L}_{PQ}) lead to a lot of clustering and more compact latent spaces.

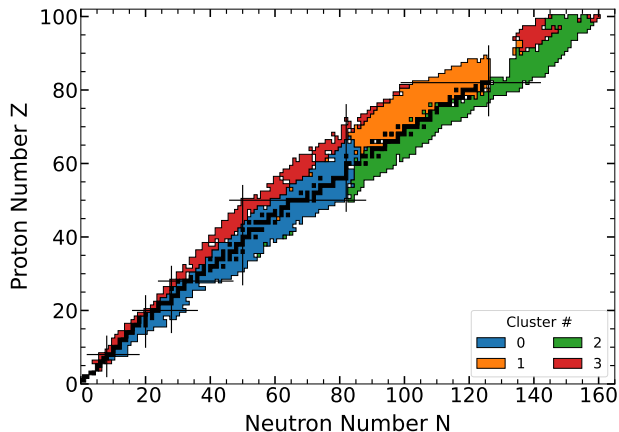


Figure 8. Location of each nucleus in the training set with color code based on which of 4 clusters the nucleus belong too. Black horizontal and vertical lines represent magic numbers. Black squares are stable nuclei.

To better analyze clustering structures, we used the `scikit-learn` implementation of the spectral clustering algorithm to identify potential clusters of points directly in the VAE or INR dataset. Out of all available clustering techniques, spectral clustering and the DBScan algorithms are the naive best choices to identify clusters based on existing documentation and literature. However, calibrating the maximum distance between any two points to be considered in the neighborhood of each other in DBScan requires a deeper understanding of the latent space than we currently have. In contrast, spectral clustering does not involve any prior knowledge of the latent space. We first determined a rough estimate of the optimal number n_{clus} of clusters based on the Silhouette method. In practice, we found $n_{\text{clus}} = 4$. Figure 8 shows the position in the nuclear chart of each nucleus from the INR encoding training dataset, color-coded by the cluster the nucleus belongs to. The most striking feature of this plot is the fact that nuclei are organized in diagonal bands loosely following the valley of stability rather than along isotopic, isotonic or isobaric sequences. In addition, some of the clusters seem to be related to neutron magic numbers (but, interestingly, not proton magic numbers), especially $N = 82$ and $N = 126$. Both observations are quite robust. In Appendix VII C, we show that different clustering scenarios lead to similar qualitative results.

B. Predictions of unknown cross sections

Predicting nuclear cross sections across the entire chart in a consistent manner and with well-defined uncertainties is particularly challenging due to the lack of experimental data on radioactive isotopes and the limited predictive power of existing models. In Section IV we have shown that both VAE and INR networks can successfully compress four-channel cross-sections with full energy index into compact, low-dimensional representations. This approach exhibits excellent encoding performance. This non-trivial result suggests that the “effective” space of nuclear cross sections is low-dimensional indeed.

The predictive ability of GNNs is dependent on the structure of the data, as observed in a supplementary experiment where we randomly sampled the TENDL graph to generate the training and test set (instead of the windowing function). In this setting the overall error across all models was higher by $\approx 30\%$. Additionally, as discussed previously, the structure of the latent space plays an important role in the optimization choice for the GNN. From Table I we see that in the case of the INR, while the ARMAConv model performs as expected, the GatedConvmodel performs worse compared to the VAE-encoding. It is important to note that the structure of the ARMAConv layer accounts for higher-order neighborhood information in the graph compared to the traditional polynomial layers used in GatedConv and GCNConv. Since ARMA filters can capture the global graph structure with a small number of learnable parameters ($\approx 250k$), it can better estimate the “islands” in the INR hypernet latent space hence providing excellent predictive ability for the test set as seen in both Fig. 4 and Fig. 5. The GatedConv model does not have this advantage and hence we observe a drop in performance for the INR-encoding.

The obvious limitation of this initial study is that the training of all networks is based on the TENDL dataset, which is itself a tabulation of predictions from a finite collection of nuclear models. However, this could be turned into an advantage: since the deep learning approach provides a single unifying representation of all cross sections in that set, cross sections that the GNN fails to reproduce and/or predict well may be used as signals for outliers in TENDL. Furthermore, our methodology can easily be extended by augmenting TENDL with additional datasets, either from evaluated libraries such as ENDF, JEFF or JENDL, or from pure experimental data such as EXFOR.

Most importantly, the learned relationships between cross sections of different types within a single nucleus, or between different nuclei can pave the way to much more ambitious studies. In the short term, short-distance extrapolation of cross sections of the type $\sigma_{\alpha}(N, Z) \rightarrow \sigma_{\alpha}(N + i, Z + j)$ for channel α should be relatively reliable, especially if i and j are small, i.e., $i, j \leq 4$. Such extrapolations would be especially useful in the context of nucleosynthesis simulations where precision matters less than accuracy. In the longer term, it should be possible to exploit these relationships to estimate covariances. Cur-

rent libraries are severely limited in covariance data and in many cases, these data are unreliable. Furthermore, cross-material covariances, that is, how uncertainties in a cross section of one nucleus are related to another type of cross section in another nucleus, have never been estimated. By providing a unified framework to compute cross sections, our methodology offers a viable path forward to estimate all such covariances and properly propagate uncertainties from nuclear data into applications. In the next section, we show how the current trained networks can already give us valuable information how uncertainties propagate across the nuclear chart.

C. Propagation of Uncertainties

To illustrate the power of our deep-learning model, we have performed the following “experiment”. We consider the $(n, 2n)$ cross section in the ^{75}As nucleus, which we note $\sigma_i(E)$, where i simply indexes the position of ^{75}As in the TENDL dataset. We generate 100 random realizations of the $\sigma_i(E)$, which we denote $\sigma_i^{(\alpha)}(E)$, by considering the covariance information listed in [29], which treats the entire evaluation as a large multivariate normal distribution. We use the VAE encoder to transform each $\sigma_i^{(\alpha)}(E)$ into a vector $\mathbf{x}_i^{(\alpha)}$ of the latent space. In the next step, we use these latent vectors $\mathbf{x}_i^{(\alpha)}$ to define new feature matrices. Keeping the notations of Section III C, we write $\mathcal{G}^{(\alpha)} = (\mathcal{V}^{(\alpha)}, \mathcal{E}^{(\alpha)})$ the graph made of nodes $\mathcal{V}^{(\alpha)}$ and edges $\mathcal{E}^{(\alpha)}$. The set of all nodes $\mathcal{V}^{(\alpha)}$ depend on the feature matrix $\mathbf{X}^{(\alpha)}$ associated with the variation α . Note that the only differences between any $\mathbf{X}^{(\alpha)}$ and $\mathbf{X}^{(\beta)}$ is the single latent vector corresponding to ^{75}As : $\mathbf{x}_i^{(\alpha)} \neq \mathbf{x}_i^{(\beta)}$. However, the trained GNN is the set of parameters that define the function χ in Eq. (4). This means that the predictions from the trained GNN for each $\mathcal{G}^{(\alpha)}$ are all different from one another: the network is unchanged but its input (=the graph $\mathcal{G}^{(\alpha)}$) is.

Let us note $\Sigma_i(E)$ the cross section *predicted* by the GNN in nucleus i based on the graph \mathcal{G} . Technically, $\Sigma_i(E)$ is obtained by running the decoder of the VAE or INR on the latent vector predicted by the GNN for that nucleus i . Since the GNN is not perfect, $\Sigma_i(E) \neq \sigma_i(E)$. Similarly, we note $\Sigma_i^{(\alpha)}(E)$ the cross section predicted by the GNN in the same nucleus i but with the input graph $\mathcal{G}^{(\alpha)}$. We can now quantify the difference in GNN predictions from any arbitrary realization α by computing the deviation

$$\varepsilon_i^{(\alpha)} = \|\Sigma_i - \Sigma_i^{(\alpha)}\|^2. \quad (9)$$

The total mean deviation across the entire TENDL dataset is then just given by $\frac{1}{n} \sum_i^n \varepsilon_i^{(\alpha)}$.

In Figure 9, we plot the deviation (9) of the GNN for each nucleus in the TENDL dataset for the variation $\alpha = 1$; similar results would be obtained for all other variations. In this experiment, the deviation should be

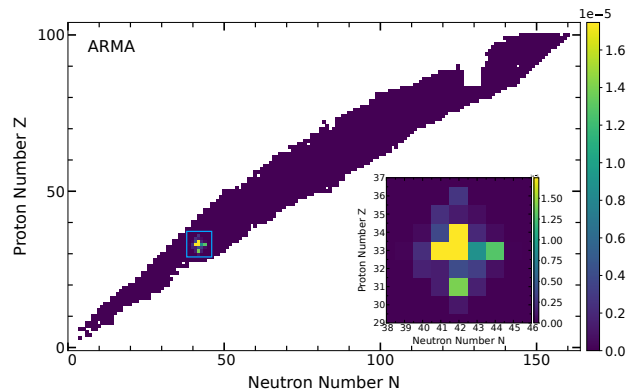


Figure 9. Deviation (9) between the GNN prediction based on the initial set of TENDL cross sections and the one based on variation $\alpha = 1$, for each nucleus in the TENDL dataset. The plot is normalized between ϵ_{\min} and $0.1 \times \epsilon_{\max}$, where ϵ_{\min} (ϵ_{\max}) is the minimum (maximum) error. The inset corresponds to the blue square centered at $Z = 33$ and $N = 42$.

thought of as a proxy to visualize the propagation of uncertainties. It shows how changes of one cross section in one nucleus propagate to neighboring nuclei. As visualized in the inset of the figure, changes are localized near the central nucleus ^{75}As and decay rapidly as we go away from this nucleus.

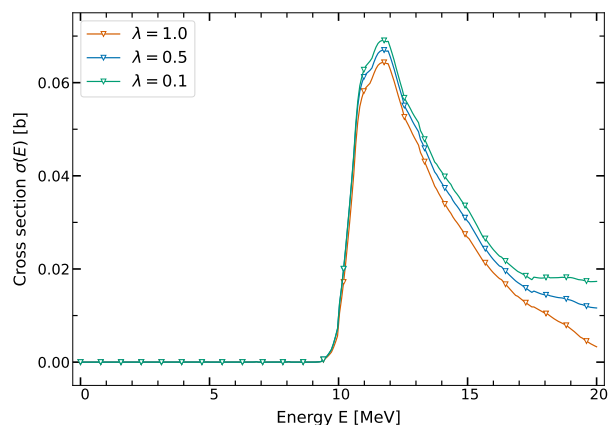


Figure 10. Deviation (9) in ^{75}As between prediction from the initial graph \mathcal{G} and three linear combinations of the first random realization $\mathcal{G}^{(1)}$; see text for details. The difference is plotted in real units (barns).

Interestingly, changes do not propagate in a linear manner through the GNN. In Fig. 10, we plot the deviation (9) by generating three different graphs from the $\alpha = 1$ variation cross section. Instead of replacing the latent vector \mathbf{x}_i by the full variation $\mathbf{x}_i^{(\alpha)}$, we first introduce “damped” variations of the cross section characterized

by the parameter λ , $\sigma_i \rightarrow \sigma_i^{(\alpha,\lambda)} = \sigma_i + \lambda(\sigma_i^{(\alpha)} - \sigma_i)$. We then encode these $\sigma_i^{(\alpha,\lambda)}$ cross sections to define the corresponding feature matrix $\mathbf{X}^{(\alpha,\lambda)}$ before running the GNN and decoding its prediction. Figure 10 was obtained for three different values $\lambda = 0.1, 0.5, 1.0$ of the damping factor. We see that the difference with the original prediction corresponding to the full variation ($\lambda = 1.0$) is in fact smaller than for the other two cases.. The reason for this behavior is that each GNN learns an unique mapping function to predict the feature vector at a specific node based on the information from the neighboring nodes. Hence, the way that information is propagated depends on the nature of the mapping function, which is not always linear. However, our method still provides crucial insight into the behavior of neighboring nuclei surrounding the perturbation site.

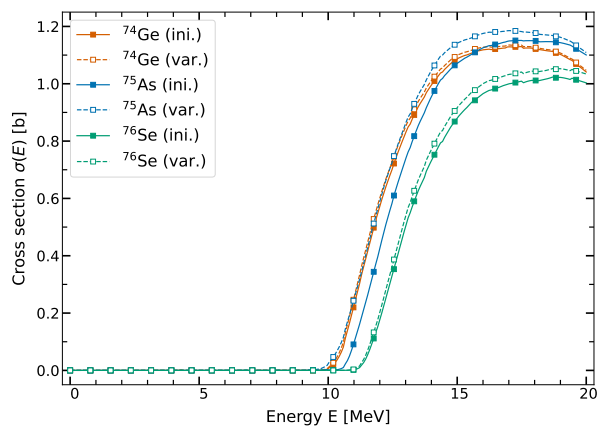


Figure 11. Predictions of the $(n, 2n)$ cross section in ^{74}Ge ($\delta Z = -1$), ^{75}As ($\delta Z = 0$), and ^{76}Se ($\delta Z = +1$) for the GNN with the initial graph \mathcal{G} (plain lines, full symbols) and the full variation $\mathcal{G}^{(1)}$ (dashed lines, open symbols). Here, δZ refers to the difference in proton number relative to ^{75}As . Cross sections are plotted in real units (barns).

Finally, to visualize the concrete impact of these variations on actual cross sections, we plot in Fig. 11 the full $(n, 2n)$ cross section as predicted by the GNN, either with the initial graph \mathcal{G} – marked as ‘ini.’ – or with the $\alpha = 1$ variation graph $\mathcal{G}^{(1)}$ – marked as ‘var.’. The plots are made for the central nucleus where the variation is generated, ^{75}As , as well as for its two nearest neighbors along the proton number axis, ^{74}Ge ($Z = 32$ and $N = 42$) and ^{76}Se ($Z = 34$ and $N = 42$).

Running the GNN on such an updated set of cross sections – in our case, the $\mathcal{G}^{(\alpha)}$ for the variations α of the $(n, 2n)$ cross section in ^{75}As – takes less than a second on a laptop. It provides an estimate of how changes in one cross section impacts all other cross sections in all other nuclei. Crucially, this information is completely agnostic: whether the changes in that cross section come from new measurements, better theories, better evaluations or a combination of the above, does not matter.

Our approach is completely data driven. As mentioned in Section II, it is simply impossible with the current state of nuclear theory and nuclear data evaluations to obtain the same information.

VI. CONCLUSION

In this work, we used variational autoencoders (VAEs) and implicit neural representations (INRs) to learn the latent space of nuclear cross sections, specifically the elastic, inelastic, $(n, 2n)$ and (n, γ) cross sections in the fast regime. Both types of architecture were trained on the synthetic data from the TENDL nuclear dataset. We then used graph neural networks (GNNs) on the latent representations to learn the relationships between these four types of cross sections. We showed that we could predict cross sections in a rather large test set with remarkably good accuracy. We also outlined how to quantify the impact new measurements or theoretical calculations would have on the GNN predictions.

Our initial results suggest that modern deep learning methods are capable of accurately predicting, in a single, unifying framework, different types of nuclear cross sections. This opens the way to a more rigorous quantification of uncertainties, especially covariances and cross-material covariances. Since experimental data on nuclear cross sections are rather scarce (at the scale of the chart of isotopes), it should be possible to augment datasets with other sources of data coming, e.g., from large-scale simulations of ground-state properties, β -decay rates and γ -strength functions, or level densities. Microscopic theories such as, e.g., nuclear density functional theory, should have enough predictive power to predict accurately the trends of these various observables at the scale of the mass table, which could in turn help constrain deep learning models during the training phase.

ACKNOWLEDGEMENTS

This work was performed under the auspices of the U.S. Department of Energy by Lawrence Livermore National Laboratory under contract DE-AC52-07NA27344. Lawrence Livermore National Security, LLC. This work was supported by the Laboratory Directed Research and Development (LDRD) program under project tracking code 23-SI-004. Computing support came from the Lawrence Livermore National Laboratory (LLNL) Institutional Computing Grand Challenge program.

VII. APPENDIX

In this section, we provide supplementary analyses and ablation studies to support the findings presented in the main paper. These experiments are designed to validate

the robustness and generalization capabilities of the proposed framework. We begin by investigating the representation learning phase with the VAE. Following this, we present the results of the downstream GNN prediction task, focusing on consistent performance across different test regions and varying window lengths.

A. Train-Test Performance Trends for VAE

To ensure that our model is not overfitting during the representation learning phase, we analyze the evolution of the loss and PSNR for both the training and testing set during the VAE training. These metrics are presented as a function of epochs in Figure 12. The training and testing loss curves show a steady decrease, converging to similar values by the end of training. Also, the PSNR values for both training and testing increase consistently, improving reconstruction quality over time. The consistent convergence of both metrics indicates minimal overfitting and robust generalization of the learned latent representations.

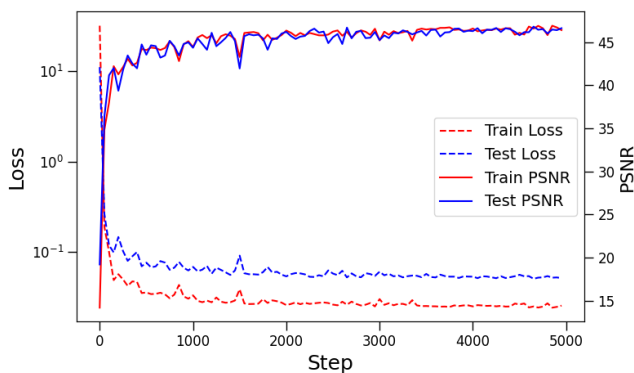


Figure 12. Loss (dashed curves) and PSNR (plain curves) for the training set (red) and testing set (blue) as a function of epoch during VAE training. Note that the y-axis for the loss is on a logarithmic scale.

B. Generalization Analysis in GNN

a. Performance consistency across test regions In the downstream prediction task with the GNN, we conduct an analysis to verify the model’s ability to generalize across different regions of the test set. To this end, we perform evaluation on multiple test regions centered on distinct nuclear chart coordinates while keeping the window length fixed (e.g., $\Delta Z = \Delta N = 8$). Figure 13 indicates that test PSNR scores across all randomly selected regions are consistent and demonstrates that the model is not biased toward specific regions of the training set. The three curves with the lowest PSNR correspond to regions centered on ^{214}Tl ($Z = 81, N = 133$), ^{219}At ($Z = 85, N = 134$) and ^{239}Pa ($Z = 91, N = 148$).

In these three cases, the TENDL library contains overall fewer isotopes of each element; see Fig. 9. As a result, the number of actual nuclei in the test set is much smaller than the 289 nuclei of most other regions. This lack of samples in these regions results in sparse relationships between neighboring nuclei compared to regions with denser neighboring points. This sparsity limits the GNN’s ability to learn comprehensive connections, leading to lower PSNR scores compared to denser test regions.

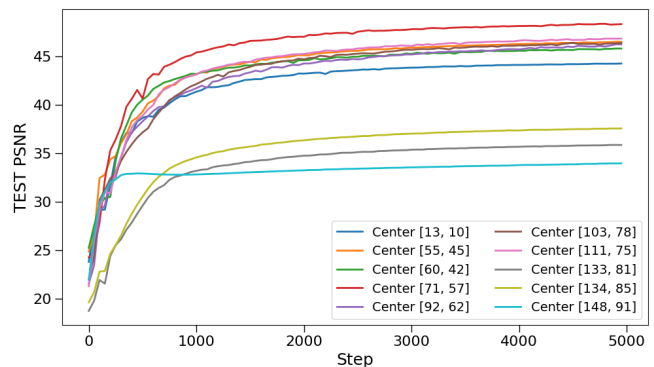


Figure 13. PSNR values in the test set as a function of epochs for test regions centered at distinct nuclear chart coordinates $[N_0, Z_0]$. All test regions have the same size characterized by $\Delta Z = \Delta N = 8$; only the center nucleus changes.

b. Performance consistency across window length variations Figure 14 shows the test PSNR scores across different window lengths for the Gated and ARMA approaches. This analysis highlights how the model performs when varying the size of the test region, where increasing the window length reduces the number of training samples available. Such a setup is crucial to evaluate the model’s ability to generalize effectively, as it forces the model to learn and infer from sparse training data. As seen in this figure, the model demonstrates robust and consistent performance across a wide range of window lengths, verifying its capability to generalize well even under challenging conditions.

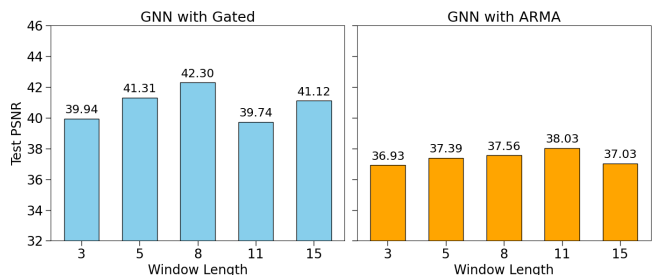


Figure 14. Test PSNR values across varying window sizes for Gated (left) and ARMA (right) approaches, with the center of the test window fixed at $(Z_0, N_0) = (42, 60)$.

C. Location of latent clusters

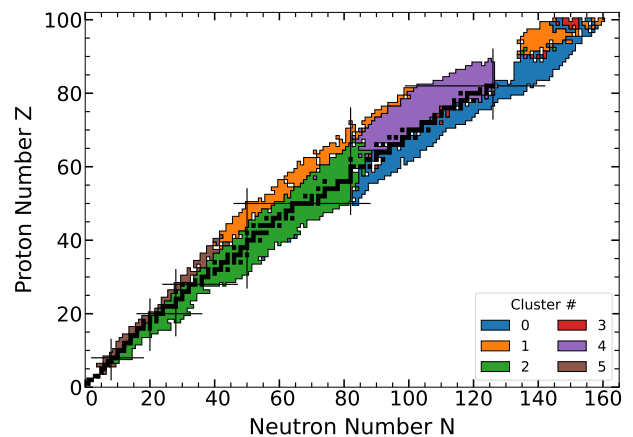


Figure 15. Location of nuclei in the training set with color code based on which cluster the nucleus belongs too. Black horizontal and vertical lines represent magic numbers. The figure corresponds to the INR latent vectors and: $n_{\text{clus}} = 6$.

Figure 16 is the exact same figure as Fig.8 in the main text, only it was constructed from the spectral clustering of the VAE latent space (with $n_{\text{clus}} = 4$). We notice that the overall “diagonal” grouping of nuclei remains, although clusters are a little less compact. In addition, the main cluster that surrounds the valley of stability is not split in two at $N = 82$ like in Fig. 8 but instead at $N = 126$. It is still interesting that neutron magic numbers seem to be identified as markers of clustering in both methods.

Finally, Fig. 17 illustrates another clustering method based on the KMeans algorithm. It is constructed from the clustering of the INR latent vectors and corresponds to $n_{\text{clus}} = 6$. Compared to Fig. 15, it illustrates the impact of a different clustering method. The KMeans method is a little more naive than spectral clustering and makes additional hypotheses about the clusters, in particular that they should be spherical. The main difference between the two methods is that KMeans produces “thinner” clusters. However, the diagonal nature of the clusters and the role of magic neutron numbers in identifying clusters remains.

In this section, we show a few more examples of the location of clusters of nuclei identified directly from the VAE or INR latent vectors. Figures 15 quantifies the impact of changing the numbers of clusters to $n_{\text{clus}} = 6$. The main change is the splitting of the cluster of proton-rich nuclei into two subsets and the appearance of a small cluster of very heavy nuclei.

-
- [1] J. Blatt and V. Weisskopf, *Theoretical Nuclear Physics* (Springer-Verlag, New York, 1979).
- [2] O. Iwamoto, N. Iwamoto, S. Kunieda, F. Minato, S. Nakayama, Y. Abe, K. Tsubakihara, S. Okumura, C. Ishizuka, T. Yoshida, S. Chiba, N. Otuka, J.-C. Sublet, H. Iwamoto, K. Yamamoto, Y. Nagaya, K. Tada, C. Konno, N. Matsuda, K. Yokoyama, H. Taninaka, A. Oizumi, M. Fukushima, S. Okita, G. Chiba, S. Sato, M. Ohta, and S. Kwon, Japanese evaluated nuclear data library version 5: JENDL-5, *J. Nucl. Sci. Technol.* **60**, 1 (2023).
- [3] A. J. M. Plompen, O. Cabellos, C. De Saint Jean, M. Fleming, A. Algora, M. Angelone, P. Archier,

E. Bauge, O. Bersillon, A. Blokhin, F. Cantargi, A. Chebboubi, C. Diez, H. Duarte, E. Dupont, J. Dyrda, B. Erasmus, L. Fiorito, U. Fischer, D. Flammini, D. Foligno, M. R. Gilbert, J. R. Granada, W. Haeck, F.-J. Hamsch, P. Helgesson, S. Hilaire, I. Hill, M. Hursin, R. Ichou, R. Jacquemin, B. Jansky, C. Jouanne, M. A. Kellett, D. H. Kim, H. I. Kim, I. Kodeli, A. J. Koning, A. Y. Konobeyev, S. Kopecky, B. Kos, A. Krása, L. C. Leal, N. Leclaire, P. Leconte, Y. O. Lee, H. Leeb, O. Litaize, M. Majerle, J. I. Márquez Damián, F. Michel-Sendis, R. W. Mills, B. Morillon, G. Noguère, M. Pecchia, S. Pelloni, P. Pereslavytsev, R. J. Perry, D. Rochman, A. Röhrmoser, P. Romain, P. Romojaro, D. Roubtsov,

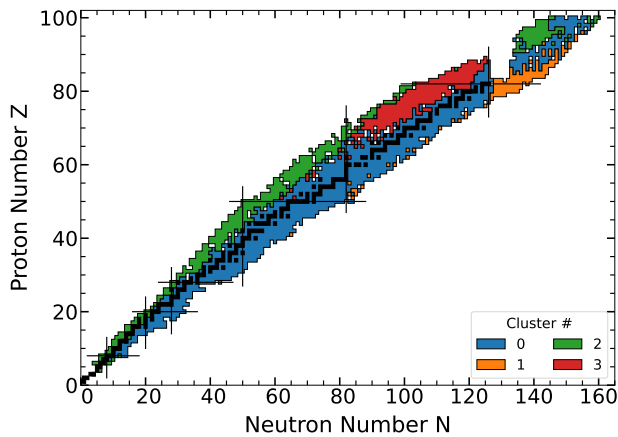


Figure 16. Same as Fig.15. The figure corresponds to the VAE latent vectors and: $n_{\text{clus}} = 4$.

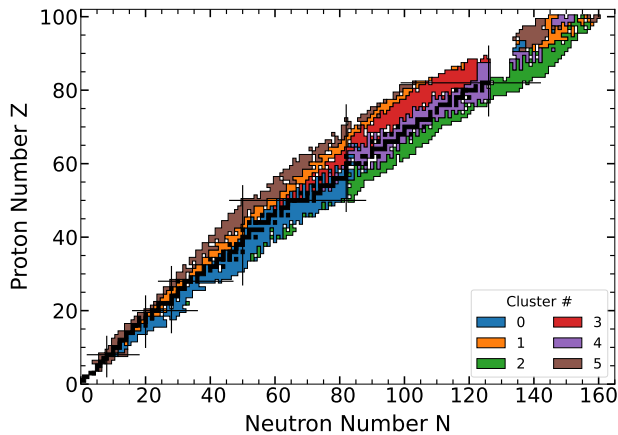


Figure 17. Same as Fig.15. The figure corresponds to the INR latent vectors and is obtained by the KMeans algorithm instead of spectral clustering and with: $n_{\text{clus}} = 6$.

P. Sauvan, P. Schillebeeckx, K. H. Schmidt, O. Serot, S. Simakov, I. Sirakov, H. Sjöstrand, A. Stankovskiy, J. C. Sublet, P. Tamagno, A. Trkov, S. van der Marck, F. Álvarez Velarde, R. Villari, T. C. Ware, K. Yokoyama, and G. Žerovnik, The joint evaluated fission and fusion nuclear data library, JEFF-3.3, Eur. Phys. J. A **56**, 181 (2020).

- [4] D. A. Brown, M. B. Chadwick, R. Capote, A. C. Kahler, A. Trkov, M. W. Herman, A. A. Sonzogni, Y. Danon, A. D. Carlson, M. Dunn, D. L. Smith, G. M. Hale, G. Arbanas, R. Arcilla, C. R. Bates, B. Beck, B. Becker, F. Brown, R. J. Casperson, J. Conlin, D. E. Cullen, M.-A. Descalle, R. Firestone, T. Gaines, K. H. Guber, A. I. Hawari, J. Holmes, T. D. Johnson, T. Kawano, B. C. Kiedrowski, A. J. Koning, S. Kopecky, L. Leal, J. P. Lestone, C. Lubitz, J. I. Márquez Damián, C. M. Mattoon, E. A. McCutchan, S. Mughabghab, P. Navratil, D. Neudecker, G. P. A. Nobre, G. Noguere, M. Paris, M. T. Pigni, A. J. Plompen, B. Pritychenko, V. G. Pronyaev, D. Roubtsov, D. Rochman, P. Romano, P. Schillebeeckx, S. Simakov, M. Sin, I. Sirakov,

B. Sleaford, V. Sobes, E. S. Soukhovitskii, I. Stetcu, P. Talou, I. Thompson, S. van der Marck, L. Welter-Sherrill, D. Wiarda, M. White, J. L. Wormald, R. Q. Wright, M. Zerkle, G. Žerovnik, and Y. Zhu, ENDF/B-VIII.0: The 8th Major Release of the Nuclear Reaction Data Library with CIELO-project Cross Sections, New Standards and Thermal Scattering Data, Nucl. Data Sheets Special Issue on Nuclear Reaction Data, **148**, 1 (2018).

- [5] L. Bernstein, F. Bostelmann, M. Carpenter, M. Chadwick, M. Fratoni, A. Hawari, L. Heilbronn, C. Howell, J. Ressler, C. Keppel, A. Koning, K. LaBel, T. Turfinger, C. Nesaraja, S. Qaim, C. Romano, A. Spyrou, S. Siem, C. Vermeulen, and R. Vogt, *First Report of the Nuclear Data Subcommittee of the Nuclear Science Advisory Committee*, Tech. Rep. LLNL-TR-840465, 1890079, 1061532 (Lawrence Livermore National Laboratory, 2022).
- [6] F. Bostelmann, G. Ilas, C. Celik, A. Holcomb, and W. Wiesquist, *Nuclear Data Assessment for Advanced Reactors*, Tech. Rep. UREG/CR-7289, ORNL/TM-2021/2002 (United States Nuclear Regulatory Commission, Washington, D.C, 2022).
- [7] M. U. Khandaker, D. A. Bradley, H. Osman, M. I. Sayyed, A. Sulieman, M. R. I. Faruque, K. A. Naseer, and A. M. Idris, The significance of nuclear data in the production of radionuclides for theranostic/therapeutic applications, Radiation Physics and Chemistry The 15th International Symposium on Radiation Physics (ISRP15), 6 - 10 December, 2021, Sunway University, Malaysia, **200**, 110342 (2022).
- [8] A. C. Hayes, Applications of nuclear physics, Rep. Prog. Phys. **80**, 026301 (2017).
- [9] I. U. Roederer, N. Vassh, E. M. Holmbeck, M. R. Mumpower, R. Surman, J. J. Cowan, T. C. Beers, R. Ezzeddine, A. Frebel, T. T. Hansen, V. M. Placco, and C. M. Sakari, Element abundance patterns in stars indicate fission of nuclei heavier than uranium, Science **382**, 1177 (2023), <https://www.science.org/doi/pdf/10.1126/science.adf1341>.
- [10] M. R. Mumpower, R. Surman, G. C. McLaughlin, and A. Aprahamian, The impact of individual nuclear properties on r-process nucleosynthesis, Prog. Part. Nucl. Phys. **86**, 86 (2016).
- [11] G. e. a. Dodge, *A new Era of Discovery: The 2023 Long-Range Plan for Nuclear Science*, Tech. Rep. (U.S. Department of Energy and National Science Foundation, 2023).
- [12] I. J. Thompson and F. M. Nunes, *Nuclear Reactions for Astrophysics: Principles, Calculation and Applications of Low-Energy Reactions* (Cambridge University Press, 2009).
- [13] P. Navrátil and S. Quaglioni, Ab Initio Nuclear Reaction Theory with Applications to Astrophysics, in *Handbook of Nuclear Physics*, edited by I. Tanihata, H. Toki, and T. Kajino (Springer Nature, Singapore, 2020) p. 1.
- [14] P. E. Hodgson, Compound nucleus reactions, Rep. Prog. Phys. **50**, 1171 (1987).
- [15] B. V. Carlson, J. E. Escher, and M. S. Hussein, Theoretical descriptions of compound-nuclear reactions: Open problems and challenges, J. Phys. G: Nucl. Part. Phys. **41**, 094003 (2014).
- [16] R. Capote, M. Herman, P. Obložinský, P. G. Young, S. Goriely, T. Belgia, A. V. Ignatyuk, A. J. Kon-

- ing, S. Hilaire, V. A. Plujko, M. Avrigeanu, O. Bersillon, M. B. Chadwick, T. Fukahori, Z. Ge, Y. Han, S. Kailas, J. Kopecky, V. M. Maslov, G. Reffo, M. Sin, E.Sh. Soukhovitskii, and P. Talou, RIPL – Reference Input Parameter Library for Calculation of Nuclear Reactions and Nuclear Data Evaluations, *Nucl. Data Sheets* **110**, 3107 (2009).
- [17] S. Goriely, P. Dimitriou, M. Wiedeking, T. Belgia, R. Firestone, J. Kopecky, M. Kr̄t̄icka, V. Plujko, R. Schwengner, S. Siem, H. Utsunomiya, S. Hilaire, S. Péru, Y. S. Cho, D. M. Filipescu, N. Iwamoto, T. Kawano, V. Varlamov, and R. Xu, Reference database for photon strength functions, *Eur. Phys. J. A* **55**, 172 (2019).
- [18] K. Kolos, V. Sobes, R. Vogt, C. E. Romano, M. S. Smith, L. A. Bernstein, D. A. Brown, M. T. Burkey, Y. Danon, M. A. Elsayi, B. L. Goldblum, L. H. Heilbronn, S. L. Hogle, J. Hutchinson, B. Loer, E. A. McCutchan, M. R. Mumpower, E. M. O’Brien, C. Percher, P. N. Peplowski, J. J. Ressler, N. Schunck, N. W. Thompson, A. S. Voyles, W. Wieselquist, and M. Zerkle, Current nuclear data needs for applications, *Phys. Rev. Research* **4**, 021001 (2022).
- [19] M. D. Schwartz, Modern Machine Learning and Particle Physics, *Harvard Data Science Review* **3** (2021), <https://hdsr.mitpress.mit.edu/pub/xqle7lat>.
- [20] HEP ML Community, A Living Review of Machine Learning for Particle Physics.
- [21] J. M. R. Fox and K. A. Wendt, Illuminating systematic trends in nuclear data with generative machine learning models (2024), arXiv:2403.16389 [nucl-th].
- [22] M. M. Bronstein, J. Bruna, Y. LeCun, A. Szlam, and P. Vandergheynst, Geometric deep learning: going beyond euclidean data, *IEEE Signal Processing Magazine* **34**, 18 (2017).
- [23] F. Scarselli, M. Gori, A. C. Tsoi, M. Hagenbuchner, and G. Monfardini, The graph neural network model, *IEEE transactions on neural networks* **20**, 61 (2008).
- [24] X. Ju, S. Farrell, P. Calafiura, D. Murnane, L. Gray, T. Klijnsmā, K. Pedro, G. Cerati, J. Kowalkowski, G. Perdue, *et al.*, Graph neural networks for particle reconstruction in high energy physics detectors, arXiv preprint arXiv:2003.11603 (2020).
- [25] C. Doersch, Tutorial on variational autoencoders, arXiv preprint arXiv:1606.05908 (2016).
- [26] Koning, Arjan, Hilaire, Stephane, and Goriely, Stephane, Talys: modeling of nuclear reactions, *Eur. Phys. J. A* **59**, 131 (2023).
- [27] M. Herman, R. Capote, B. V. Carlson, P. Obložinský, M. Sin, A. Trkov, H. Wienke, and V. Zerkin, EMPIRE: Nuclear Reaction Model Code System for Data Evaluation, *Nucl. Data Sheets Special Issue on Evaluations of Neutron Cross Sections*, **108**, 2655 (2007).
- [28] M. Bender, P.-H. Heenen, and P.-G. Reinhard, Self-consistent mean-field models for nuclear structure, *Rev. Mod. Phys.* **75**, 121 (2003).
- [29] A. J. Koning, D. Rochman, J. C. Sublet, N. Dzysiuk, M. Fleming, and S. van der Marck, TENDL: Complete Nuclear Data Library for Innovative Nuclear Science and Technology, *Nucl. Data Sheets Special Issue on Nuclear Reaction Data*, **155**, 1 (2019).
- [30] D. P. Kingma and M. Welling, Auto-encoding variational bayes, arXiv preprint arXiv:1312.6114 (2013).
- [31] D. Ha, A. M. Dai, and Q. V. Le, Hypernetworks, in *International Conference on Learning Representations* (2016).
- [32] V. Sitzmann, J. Martel, A. Bergman, D. Lindell, and G. Wetzstein, Implicit neural representations with periodic activation functions, *Advances in neural information processing systems* **33**, 7462 (2020).
- [33] M. I. Jordan, Z. Ghahramani, T. S. Jaakkola, and L. K. Saul, An introduction to variational methods for graphical models, *Machine learning* **37**, 183 (1999).
- [34] A. F. Agarap, Deep learning using rectified linear units (relu), arXiv preprint arXiv:1803.08375 (2018).
- [35] B. Mildenhall, P. P. Srinivasan, M. Tancik, J. T. Barron, R. Ramamoorthi, and R. Ng, Nerf: Representing scenes as neural radiance fields for view synthesis, *Communications of the ACM* **65**, 99 (2021).
- [36] L. Mescheder, M. Oechsle, M. Niemeyer, S. Nowozin, and A. Geiger, Occupancy networks: Learning 3d reconstruction in function space, in *Proceedings of the IEEE/CVF conference on computer vision and pattern recognition* (2019) pp. 4460–4470.
- [37] F. Szatkowski, K. J. Piczak, P. Spurek, J. Tabor, and T. Trzciński, Hypernetworks build implicit neural representations of sounds, in *Joint European Conference on Machine Learning and Knowledge Discovery in Databases* (Springer, 2023) pp. 661–676.
- [38] J. Gilmer, S. S. Schoenholz, P. F. Riley, O. Vinyals, and G. E. Dahl, Neural message passing for quantum chemistry, in *International conference on machine learning* (PMLR, 2017) pp. 1263–1272.
- [39] F. M. Bianchi, D. Grattarola, L. Livi, and C. Alippi, Graph neural networks with convolutional arma filters, *IEEE transactions on pattern analysis and machine intelligence* **44**, 3496 (2021).
- [40] Y. Li, D. Tarlow, M. Brockschmidt, and R. Zemel, Gated graph sequence neural networks, arXiv preprint arXiv:1511.05493 (2015).
- [41] T. N. Kipf and M. Welling, Semi-supervised classification with graph convolutional networks, arXiv preprint arXiv:1609.02907 (2016).
- [42] Z. Zhang, Improved adam optimizer for deep neural networks, in *2018 IEEE/ACM 26th international symposium on quality of service (IWQoS)* (Ieee, 2018) pp. 1–2.
- [43] L. van der Maaten and G. Hinton, Visualizing Data using t-SNE, *J. Mach. Learn. Res.* **9**, 2579 (2008).
- [44] J.-i. Katakura, *JENDL FP Decay Data File 2011 and Fission Yields Data File 201*, Tech. Rep. 2011-025 (Japan Atomic Energy Agency, 2012).
- [45] A. Santamarina, D. Bernard, P. Blaise, M. Coste, A. Courcelle, T. D. Huynh, C. Jouanne, P. Leconte, O. Litaize, S. Mengelle, *et al.*, The JEFF-3.1. 1 nuclear data library, *JEFF Rep.* **22**, 2 (2014).
- [46] A. J. Koning, S. Hilaire, and M. C. Duijvestijn, TALYS-1.0, in *Proc. Int. Conf. Nucl. Data Sci. Technol.* (EDP Sciences, Nice, France, 2008) p. 211.
- [47] A. J. Koning and D. Rochman, Modern Nuclear Data Evaluation with the TALYS Code System, *Nucl. Data Sheets Special Issue on Nuclear Reaction Data*, **113**, 2841 (2012).
- [48] R. J. Gladstone, H. Rahmani, V. Suryakumar, H. Meidani, M. D’Elia, and A. Zareei, Gnn-based physics solver for time-independent pdes, arXiv preprint arXiv:2303.15681 (2023).
- [49] A. Vaswani, N. Shazeer, N. Parmar, J. Uszkoreit, L. Jones, A. N. Gomez, L. Kaiser, and I. Polosukhin, At-

- tention is all you need, *Advances in neural information processing systems* **30** (2017).
- [50] J.-Y. Zhu, T. Park, P. Isola, and A. A. Efros, Unpaired image-to-image translation using cycle-consistent adversarial networks, in *Proceedings of the IEEE international conference on computer vision* (2017) pp. 2223–2232.
- [51] C. Zhang, J. Bütepage, H. Kjellström, and S. Mandt, Advances in variational inference, *IEEE transactions on pattern analysis and machine intelligence* **41**, 2008 (2018).